SCIENTIFIC REPORTS

Correction: Publisher Correction

OPEN

Tamm plasmon modes on semi-infinite metallodielectric superlattices

Received: 28 February 2017
Accepted: 26 April 2017
Published online: 16 June 2017

Goran Isić[1], Slobodan Vuković[2,3], Zoran Jakšić[2] & Milivoj Belić[3]

We analyze the fundamental properties of optical waves referred to as Tamm plasmon modes (TPMs) which are tied to the interface of a semi-infinite two-phase metallodielectric superlattice with an arbitrary homogeneous capping medium. Such modes offer new ways of achieving high electromagnetic field localization and spontaneous emission enhancement in the vicinity of the interface in conjunction with absorption loss management, which is crucial for future applications. The homointerface, formed when the capping medium has the same permittivity as one of the superlattice constituents, is found to support a TPM whose dispersion overlaps the single-interface surface plasmon polariton (SPP) dispersion but which has a cut off at the topological transition point. In contrast, a heterointerface formed for an arbitrary capping medium, is found to support multiple TPMs whose origin can be traced by considering the interaction between a single-interface SPP and the homointerface TPM burried under the top layer of the superlattice. By carrying out a systematic comparison between TPMs and single-interface SPPs, we find that the deviations are most pronounced in the vicinity of the transition frequency for superlattices in which dielectric layers are thicker than metallic ones.

The development of nanofabrication techniques has recently enabled the experimental demonstration of various artificial materials consisting of subwavelength metallodielectric elements - metamaterials, designed to exhibit peculiar optical properties that are not present in conventional media[1]. Aimed at gaining control over light propagation, any artificial optical material must rely on a high radiation confinement and low losses in the structure composites[2]. Surface modes on metal-dielectric interfaces offer a high radiation confinement to the surface, but the presence of intrinsic dissipation in the metallic component imposes severe restrictions to their applications.

Among a variety of metamaterials that have been designed and fabricated so far, the so-called hyperbolic metamaterials (HMMs) have attracted a rapidly growing attention[3], as high quality ultrathin metal films can be grown[4] yielding metallodielectric superlattices that support electromagnetic modes with very high wavenumbers and large photonic density of states that enables unprecedented ability to access and manipulate the near-field coming from a light emitter or a scattering source[5,6]. HMMs can be composed of alternating metal and dielectric layers, of an array of metallic nanowires embedded in a dielectric and different other 2D and 3D metal-dielectrics[7].

The aim of the present paper is to investigate the fundamental properties of surface plasmon modes localized at the planar interface between an arbitrary semi-infinite medium, metal or dielectric, with a semi-infinite metallodielectric superlattice. The term superlattice is used to emphasize the periodic arrangement of alternating metal and dielectric layers. Because of the analogy with electronic states localized at crystal lattice interfaces, we refer to these surface waves as Tamm plasmon modes (TPM). Surface optical waves at an interface between a metal and a purely dielectric superlattice (i.e. dielectric Bragg mirror), here referred to as Bragg TPMs, have been considered previously[8–10]. The fact that such Tamm plasmons appear within the dielectric light cones in both s- and p-polarization, inside the band gap of the Bragg mirror, makes them interesting for applications in lasers[11], photodetectors[12], engineering of spontaneous optical emission[10] and chemical and biological refractometric sensors[13,14].

[1]Institute of Physics Belgrade, Center for Solid State Physics and New Materials, University of Belgrade, Belgrade, 11080, Serbia. [2]Institute of Chemistry, Technology and Metallurgy, Center Of Microelectronic Technologies, University of Belgrade, Belgrade, 11000, Serbia. [3]Texas A&M University at Qatar, Doha, P.O. Box 23874, Qatar. Correspondence and requests for materials should be addressed to G.I. (email: isicg@ipb.ac.rs)

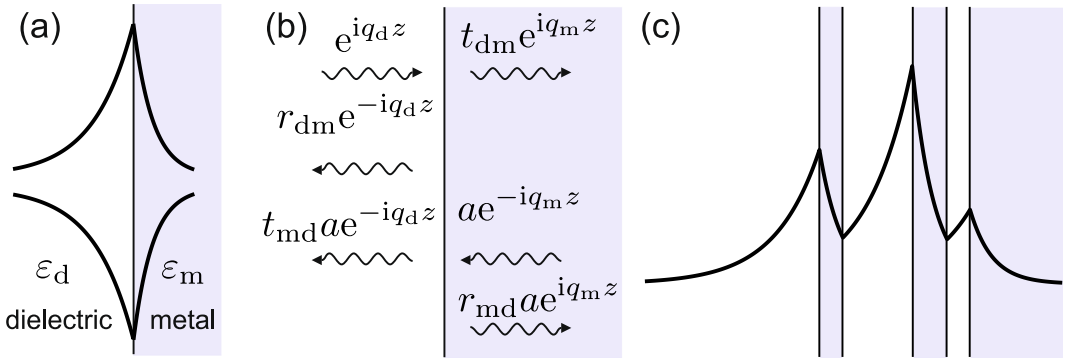

Figure 1. Schematics showing the general properties of stratified two-phase metallodielectric systems with an odd number of interfaces. (**a**) Two possible magnetic field variations which fulfill the interface boundary conditions. (**b**) Definition of Fresnel reflection and transmission coefficients. (**c**) Magnetic field of a mode fulfilling both the interface and boundary conditions at infinity.

In contrast to Bragg TPMs, the dispersion curves of metallodielectric TPMs have not been discussed systematically in literature so far. Metallodielectric TPMs are related to the traditional surface plasmon polaritons (SPPs) in that they are in-plane, p-polarized evanescent waves, but they stem from the hybridization of many single-interface SPPs of the metallodielectric superlattice and dielectric gap polaritons. The TPMs lie outside the dielectric light cone like the conventional SPPs and thus cannot escape from the flat interface, they appear when both the dielectric and metal layers are deeply subwavelength and have finite lateral group velocities. An important difference between Bragg and metallodielectric TPMs, perhaps crucial for tailoring spontaneous emission, is that the later exist even at the interface with air while the former are always buried beneath the interface with the Bragg mirror.

The current relevance of metallodielectric TPMs comes from recent reports on spontaneous emission enhancement by metallodielectric superlattices[15–17] from which it is evident that they strongly affect the photonic density of states of an interface although a systematic understanding of their role is still lacking.

We analyze the conditions for the TPM existence for both metallic and dielectric capping layers, and determine their dispersion, propagation lengths as well as the TPM resonance strength quantified by the reflection coefficient residue at the TPM pole, which is proportional to the power a point dipole placed close to the interface would emit into the mode[18]. We also analyze the predictions made within the effective medium approximation (EMA), which becomes accurate in the limit of vanishing layer thicknesses.

Two-phase stratified systems. We start with a reasoning requiring the use of single-interface boundary conditions only with minimal technical details. In spite of its deceptively simple appearance, it allows us to reach a general result regarding the existance of a particular surface mode in an arbitrary two-phase metallodielectric system and offers the explanation for some surprisingly simple properties of homointerface TPMs. A rigorous transfer-matrix-based method is then used in the remainder of the paper to confirm the general statements of this section for the particular case of a two-phase system involving a semi-infinite metallodielectric superlattice whose periodicity allows us to find closed-form solutions at the homointerface.

Starting from macroscopic Maxwell equations in which a dielectric and metallic medium are characterized by relative dielectric permittivities ε_d and ε_m, the boundary conditions imposed on a p-polarized surface wave on the planar interface between two media, with transverse wavevector components q_i ($i = \mathrm{d}, \mathrm{m}$), are found to imply[2]

$$\alpha_d + \alpha_m = 0, \quad \alpha_i = \frac{q_i}{\varepsilon_i}, \quad i = \mathrm{d}, \mathrm{m}. \tag{1}$$

Assuming that the z-axis is perpendicular to the interface and oriented towards the metallic medium, the fields of the surface wave are proportional to $\exp(-iq_d z)$ and $\exp(iq_m z)$, in the dielectric and metal medium respectively, from which it follows that the imaginary parts of both q_i must be positive in order to meet boundary conditions at infinity. This case corresponds to a magnetic field whose magnitude has a peak at the interface, as indicated by the top curve in Fig. 1(a).

However, Eq. (1) remains fulfilled if q_i are both replaced by $-q_i$, corresponding to fields growing exponentially away from the local minimum at interface, as depicted by the bottom curve in Fig. 1(a).

Introducing the Fresnel reflection and transmission coefficients as

$$r_{dm} = \frac{\alpha_d - \alpha_m}{\alpha_d + \alpha_m}, \quad t_{dm} = 1 + r_{dm}, \tag{2}$$

for incidence from the dielectric side, and

$$r_{md} = -r_{dm}, \quad t_{md} = 1 + r_{md} = 1 - r_{dm}, \tag{3}$$

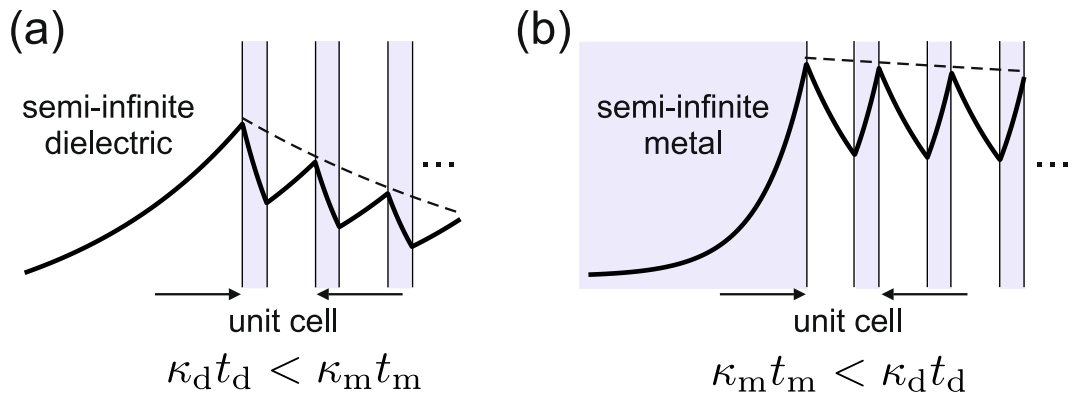

Figure 2. Magnetic field variation on homointerfaces for (**a**) dielectric and (**b**) metallic capping medium. The requirement that the Bloch anvelope, indicated by dashed lines, decays towards infinity on the right, yield the condition that $\kappa_d t_d < \kappa_m t_m$ and $\kappa_d t_d > \kappa_m t_m$ for (**a**,**b**), respectively. Note that the values of κ_d and κ_m used in panels (**a**,**b**) differ.

for the opposite incidence, the case of field having the peak at the interface is seen to represent the scattered field for an incoming wave from either medium, when $|r_{dm}|$ diverges, which is equivalent[19] to Eq. (1).

The analogous explanation of how the solution growing away from the interface arises, is found by assuming two waves are incident on the interface, the one from the dielectric side with unit amplitude and the other with complex amplitude a, as depicted in Fig. 1(b). By chosing $a = r_{dm}/(r_{dm} - 1)$, the fields going away from the interface cancel out when r_{dm} has a pole, leaving only the incoming components which correspond to the exponential growth away from the interface.

The significance of the latter solution to interface boundary conditions becomes apparent when additional layers with permittivities ε_d and ε_m are inserted between the semi-infinite dielectric and metal media, which means adding an even number of interfaces to the initial one. Now it is seen that if the boundary conditions at each interface are satisfied by alternating field maxima and minima, as depicted in Fig. 1(c), the boundary conditions at infinity will also be fulfilled, meaning that the obtained field will represent a surface mode of the multilayer. Therefore, any metallodielectric multilayer capped by the semi-infinite dielectric on one side and the metallic medium on the other, will have at least one surface mode whose transverse wavevector components fulfill Eq. (1), which implies that its dispersion curve is identical with the single-interface SPP dispersion curve

$$\beta_{dm} = k_0 \sqrt{\frac{\varepsilon_d \varepsilon_m}{\varepsilon_d + \varepsilon_m}}, \tag{4}$$

where β_{dm} represents the complex amplitude of the longitudinal (parallel to interfaces) wavevector component and $k_0 = \omega/c$ is the free-space wavenumber.

To see the implications of this general result for semi-infinite metallodielectric superlattices, we consider a surface wave, henceforth referred to as TPM, with a dispersion given by Eq. (4). The first condition it has to satisfy on a semi-infinite superlattice capped by a dielectric, as depicted in Fig. 2(a), is that it decays exponentially to the left, meaning that moving to the right, it has to decay in metallic layers and grow in dielectric ones. Denoting by t_i the layer thicknesses and κ_i the imaginary part of q_i, we see that the field amplitude is multiplied by $\exp(-\kappa_m t_m)$ and $\exp(\kappa_d t_d)$ in passing through the metal and the dielectric layer, respectively, meaning that passing through one unit cell, its amplitude is multiplied by $\exp(-\kappa_m t_m + \kappa_d t_d)$. The second condition imposed on this TPM is that it decays towards infinity on the right side, therefore a TPM on the dielectric-capped superlattice can exist only if

$$\kappa_d t_d < \kappa_m t_m. \tag{5}$$

Repeating the above reasoning for the metal-capped superlattice, the field amplitude is seen to be multiplied by $\exp(\kappa_m t_m - \kappa_d t_d)$ in passing each unit cell, so a TPM with dispersion given by Eq. (4) will exist if the opposite is true

$$\kappa_d t_d > \kappa_m t_m. \tag{6}$$

In the following section we show rigorously that the homointerface supports only the TPMs given by Eq. (4), in conjunction with conditions (5) or (6), depending on the capping medium. Under such circumstances, the reasoning applied in this section has a purpose of giving an intuitive explanation of several coincidences that might not have been expected. One interesting point to note here is that if the two possible homointerfaces of a given semi-infinite superlattice are considered, one being capped by the dielectric and the other by the metal constituent medium as in Fig. 2(a) and (b), at any given frequency ω only one of the conditions in Eqs. (5) or (6) can be fulfilled, so only one of them can support a TPM. This hints that in drawing the schematics in Fig. 2, different values of ω have been assumed for panels (a) and (b).

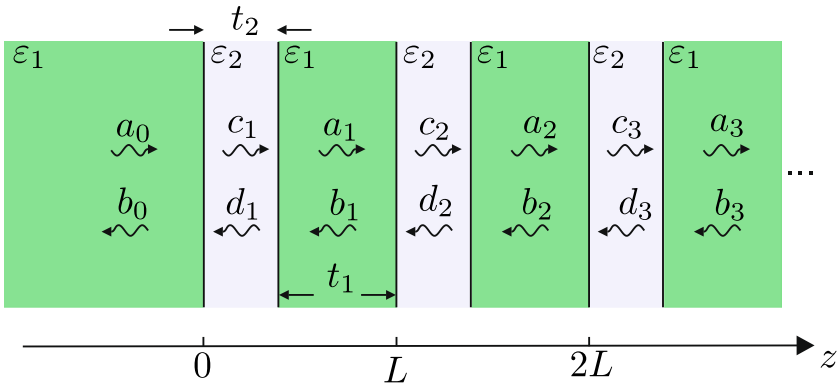

Figure 3. Schematics of the homointerface geometry used in the transfer-matrix method. The ε_1 medium extends from left infinity up to the interface at $z=0$, after which the superlattice is formed by periodically repeating the unit cell comprising a ε_2 and ε_1 layer.

Homointerface. The general geometry of the problem is sketched in Fig. 3. The capping medium permittivity is assumed equal to one of the lattice constituents, ε_1, while the second medium permittivity is ε_2. This system will henceforth be referred to as homointerface. In determining the fields, we follow the transfer-matrix method of ref.[20] For completeness and due to some minor differences in notation, here we briefly summarize the main aspects of the method.

The trasverse field phasor F in the n-th unit cell is represented as a sum of the forward and backward propagating plane wave amplitudes, denoted by a_n and b_n in medium ε_1 and by c_n and d_n in the second medium. F corresponds to the electric or magnetic field for a s- or p-polarized wave, respectively. The wave amplitudes a_n, b_n of adjacent unit cells are related by the translation matrix

$$\begin{bmatrix} a_{n-1} \\ b_{n-1} \end{bmatrix} = T \begin{bmatrix} a_n \\ b_n \end{bmatrix}, \quad T = \begin{bmatrix} A & B \\ C & D \end{bmatrix}, \tag{7}$$

whose elements are given by

$$A = \mathrm{e}^{-\mathrm{i}q_1t_1}\left[\cos(q_2t_2) - \frac{\mathrm{i}}{2}\left(\frac{\alpha_2}{\alpha_1} + \frac{\alpha_1}{\alpha_2}\right)\sin(q_2t_2)\right], \tag{8}$$

$$B = -\mathrm{e}^{\mathrm{i}q_1t_2}\frac{\mathrm{i}}{2}\left(\frac{\alpha_2}{\alpha_1} - \frac{\alpha_1}{\alpha_2}\right)\sin(q_2t_2), \tag{9}$$

$$C = \mathrm{e}^{-\mathrm{i}q_1t_2}\frac{\mathrm{i}}{2}\left(\frac{\alpha_2}{\alpha_1} - \frac{\alpha_1}{\alpha_2}\right)\sin(q_2t_2), \tag{10}$$

$$D = \mathrm{e}^{\mathrm{i}q_1t_1}\left[\cos(q_2t_2) + \frac{\mathrm{i}}{2}\left(\frac{\alpha_2}{\alpha_1} + \frac{\alpha_1}{\alpha_2}\right)\sin(q_2t_2)\right]. \tag{11}$$

Here q_i represent the complex wavector z-components, related with the longitudinal (in-plane) component β via the dispersion relation of each layer

$$q_i = \pm\sqrt{\varepsilon_i k_0^2 - \beta^2}, \quad \mathrm{Im}\{q_i\} \geq 0, \tag{12}$$

with $\pm$ denoting the sign that gives q_i with a non-negative imaginary part. In case of s-polarization, $\alpha_i = q_i$ while for p-polarization $\alpha_i = q_i/\varepsilon_i$, as before.

From the above, T is seen to be unimodular for any (real or complex) ε_i or q_i. It further implies that the product of its two eigenvalues is unity, so they can be written in the form $\mathrm{e}^{\pm\mathrm{i}KL}$, where $L = t_1 + t_2$ and K is the Bloch wavenumber. Here we define K so that $\exp(\mathrm{i}KL)$ corresponds to a wave propagating towards positive infinity, meaning that

$$\mathrm{e}^{\mathrm{i}KL} = \frac{A+D}{2} \pm \sqrt{\left(\frac{A+D}{2}\right)^2 - 1}, \quad \mathrm{Im}\{K\} \geq 0, \tag{13}$$

where $\pm$ denotes the sign giving a non-negative imaginary part of K.

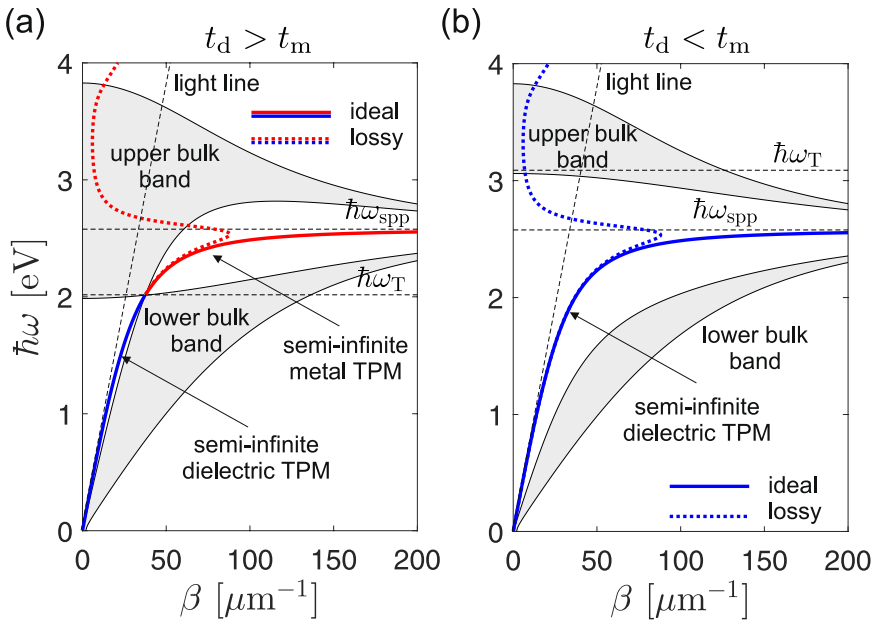

Figure 4. Bulk band structure (shading) and TPMs (thick lines) of one typical example for each the two possible band structure topologies. (**a**) $t_d > t_m$ with $\omega_T < \omega_{spp}$, leading to an intersection of the bands at ω_T. Here titanium dioxide and silver are assumed with $t_d = 20$ nm and $t_m = 10$ nm. (**b**) $t_d > t_m$ leading to $\omega_T < \omega_{spp}$ meaning that the upper and lower bulk bands do not intersect. Here $t_d = 10$ nm and $t_m = 20$ nm is assumed for titanium dioxide and silver, respectively.

Before proceeding further, the basic aspects of dissipation should be clarified. At visible and infrared frequencies, the dominant source of dissipation, by far, are intra- and inter-band electronic transitions in the metal. Therefore, we assume that the dielectric has a purely real relative permittivity $\varepsilon_d = 6.76$, corresponding to titanium dioxide, while for metal we use the silver Drude-Lorentz parametrized experimental data from ref.[21]. A convenient method[22] to treat the problem of losses is to introduce a modified dielectric function of the metal via the perturbation parameter p

$$\varepsilon_m^{(p)} = \mathrm{Re}\{\varepsilon_m\} + ip\mathrm{Im}\{\varepsilon_m\}, \quad \varepsilon_m^{(1)} \triangleq \varepsilon_m. \tag{14}$$

Setting p to unity recovers the original ε_m, while reducing it towards zero approaches smoothly the lossless case $\varepsilon_m^{(0)}$ in which the optical eigenmodes can properly be defined. The latter are thus used as a convenient scaffold on which quantities calculated with real loss are projected. The eigenmodes of a lossless infinite superlattice, henceforth referred to as bulk modes, are defined as solutions of Eq. (13) having both their eigenfrequency ω and wavevector $\mathbf{k} = (\beta, K)$ purely real.

Depending on the relative thickness of the dielectric, t_d, and metal, t_m, layers, the band structure of the infinite superlattice is known to have one of two possible topologies, corresponding to $t_d > t_m$ and $t_d < t_m$, as indicated by the shaded areas in Fig. 4(a) and (b). In this paper we carry out concrete calculations for one representative example from both classes: $t_d = 20$ nm, $t_d = 10$ nm, shown in Fig. 4(a), and $t_d = 10$ nm, $t_m = 20$ nm, in Fig. 4(b).

A general property of the $t_d > t_m$ class is that the upper and lower bulk bands intersect[23] at a frequency ω_T we shall refer to as the transition frequency. In the literature, ω_T is sometimes[15] referred to as the topological transition point since the band topology changes when crossing ω_T. It can be shown[23] that ω_T is defined by the condition

$$t_d\varepsilon_d + t_m\varepsilon_m(\omega_T) = 0, \tag{15}$$

which can alternatively be stated as

$$\varepsilon_\parallel(\omega_T) = 0, \tag{16}$$

with $\varepsilon_{||}$ denoting the average in-plane permittivity (or the in-plane permittivity tensor component in EMA)

$$\varepsilon_\parallel = \eta\varepsilon_1 + (1 - \eta)\varepsilon_2, \quad \eta = \frac{t_1}{L}. \tag{17}$$

While it is obvious that ω_T can be engineered by varying the thickness of layers in the metallodielectric superlattice, it is interesting that its value does not depend on the actual layer thicknesses but only on their ratio t_d/t_m.

The bulk bands of the $t_d < t_m$ class are separated by $\beta_{dm}(\omega)$ which lies between them. The band edges shown by thin (black) lines in Fig. 4 correspond to solutions having $\cos(KL) = 1$ (inner boundaries) and $\cos(KL) = -1$ (outer boundaries). In a lossy system, however, there is no strict definition of band edges, but rather a continuum

of modes in the $\beta-\omega$ plane whose lifetime and propagation lengths increase rapidly around the band edges of the lossless system[22].

Having defined the bulk bands of the superlattice, we are now ready to discuss the surface modes of the semi-infinite superlattice, i.e. the TPMs. By definition, the surface mode at a planar interface must be located outside the bulk bands of both the capping medium and the superlattice, meaning that it must be represented by a point in the $\beta-\omega$ plane outside both the light line and the shaded regions in Fig. 4.

TPMs are identified as poles of the reflection coefficient r of an incoming wave from the capping layer. The reflection coefficient r for the semi-infinite superlattice is determined as the $N\rightarrow\infty$ limit of the reflection coefficient r_N of a system comprising N unit cells, such that the ε_1 medium of the N-th unit cell is semi-infinite. In that case[20], a_N, b_N are related with a_0, b_0 via T^N while r_N is defined as the ratio of b_0 and a_0 when there is no incoming wave in the N-th layer. Using the known expression[24] for T^N, we find

$$r_N = \frac{C}{A - \sin([N-1]KL)/\sin(NKL)}, \tag{18}$$

with A and C given by Eqs. (8) and (10). Remembering that K has at least an infinitesimaly small positive imaginary part, we find

$$\lim_{N\rightarrow\infty}\frac{\sin([N-1]KL)}{\sin(NKL)} = \mathrm{e}^{\mathrm{i}KL}, \tag{19}$$

and finally

$$r = \lim_{N\rightarrow\infty} r_N = \frac{C}{A - \mathrm{e}^{\mathrm{i}KL}}. \tag{20}$$

The condition for the existence of a TPM is that r diverges which happens when

$$A = \mathrm{e}^{\mathrm{i}KL}. \tag{21}$$

Combining Eq. (13) with Eqs. (8) and (11), the necessary condition for Eq. (21) to hold in a non-trivial case is found to be

$$\alpha_1 + \alpha_2 = 0. \tag{22}$$

Since this is equivalent with Eq. (1), a TPM can exist only in p-polarization while its in-plane wavenumber must be qual to that of the single-interface SPP $\beta_{\mathrm{TPM}}(\omega)=\beta_{\mathrm{md}}(\omega)$.

Combining Eqs. (21) and (22) for p-polarization gives

$$K = \frac{q_2t_2 - q_1t_1}{L} = -\alpha_1\varepsilon_{\|} = \alpha_2\varepsilon_{\|}. \tag{23}$$

Since K has a non-negative imaginary part by definition, we find that a TPM can exist on a homointerface only if

$$\mathrm{Im}\{-\alpha_1\varepsilon_{\|}\} = \mathrm{Im}\{\alpha_2\varepsilon_{\|}\} \geq 0. \tag{24}$$

For a dielectric-capped homointerface, where $\varepsilon_1=\varepsilon_{\mathrm{d}}$, Eq. (24) requires $\varepsilon_{\|}$ to be negative in the lossless limit, meaning that the TPM exist only for frequencies up to ω_{T}, as indicated by the thick solid blue curves in Fig. 4(a) and (b). In contrast, the metal-capped homointerface, where $\varepsilon_1=\varepsilon_{\mathrm{m}}$, supports a TPM only above ω_{T} as $\varepsilon_{\|}$ must be positive. As ω_{T} is below the surface plasmon resonance frequency ω_{spp} (the upper frequency limit for SPP propagation), only if $t_{\mathrm{d}}>t_{\mathrm{m}}$, a TPM on a metal-capped homointerface exists only in the $t_{\mathrm{d}}>t_{\mathrm{m}}$ class of superlattices, as indicated by the thick solid red line in Fig. 4(a).

Solving for Eqs. (22) and (24) with loss taken into account yields complex values for $\beta_{\mathrm{TPM}}(\omega)$, the real part of which is drawn in Fig. 4(a) and (b) by thick dotted lines. We find that, quite generally, at any given frequency ω a TPM mode with $\beta_{\mathrm{TPM}}(\omega)=\beta_{\mathrm{md}}(\omega)$ exists either on the metal- or dielectric capped superlattice, which is manifested by the fact that taken together, they form the complete SPP dispersion curves $\beta_{\mathrm{dm}}(\omega)$ in Fig. 4(a) and (b). In the lossy case, some subtleties arise regarding the inequality in Eq. (24), as indicated by the fact that the metal-capped $t_{\mathrm{d}}>t_{\mathrm{m}}$ homointerface is found to support a TPM above around 3.82 eV. Such modes, however, exist only formally as their lifetimes are way too short to be relevant.

The above transfer-matrix-based homointerface TPM analysis thus shows formally that the TPM eigenmodes discussed on general grounds in Section "Two-phase stratified systems" are, in fact, the only possible surface modes and that they have properties very similar to single-interface SPPs. Before proceeding with details showing the important differences between the two, we briefly look at the problem from the EMA perspective.

In EMA, the layer thicknesses t_i are assumed to be negligible relative to any length scale relevant for wave propagation, so the superlattice is described by two dielectric permittivities $\varepsilon_{\|}$ and $\varepsilon_{\perp}$, with the former having been defined previously in Eq. (17) and the latter given by

$$\varepsilon_{\perp} = \frac{\varepsilon_1\varepsilon_2}{(1-\eta)\varepsilon_1 + \eta\varepsilon_2}. \tag{25}$$

The reflection coefficient for a p-polarized wave incident from a semi-infinite medium ε_1 is

$$r_{\mathrm{ema}} = \frac{\alpha_1 - \alpha_{\mathrm{ema}}}{\alpha_1 + \alpha_{\mathrm{ema}}}, \quad \alpha_{\mathrm{ema}} = \frac{q_{\mathrm{ema}}}{\varepsilon_{\parallel}}, \tag{26}$$

while the transverse wavenumber in the effective uniaxial medium is

$$q_{\mathrm{ema}} = \pm \sqrt{\varepsilon_{\parallel} k_0^2 - \frac{\varepsilon_{\parallel}}{\varepsilon_{\perp}} \beta^2}, \quad \mathrm{Im}\{q_{\mathrm{ema}}\} \geq 0. \tag{27}$$

The dispersion of the surface mode at the interface between ε_1 and the uniaxial medium is obtained as

$$\beta_{\mathrm{ema}} = \pm\, k_0 \sqrt{\frac{\varepsilon_1 \varepsilon_{\perp} (\varepsilon_{\parallel} - \varepsilon_1)}{\varepsilon_{\parallel} \varepsilon_{\perp} - \varepsilon_1^2}}, \quad \mathrm{Im}\{\beta_{\mathrm{ema}}\} \geq 0. \tag{28}$$

Replacing $\varepsilon_{\parallel}$ and $\varepsilon_{\perp}$ by expressions given by Eqs. (17) and (25), we find that $\beta_{\mathrm{ema}} = \beta_{\mathrm{dm}}$. Since the divergence of r_{ema} requires $q_{\mathrm{ema}} = -\alpha_1 \varepsilon_{\parallel}$, a comparison with Eq. (23), shows that the perpendicular component of the wave in EMA is equal to the Bloch wavenumber

$$K = q_{\mathrm{ema}}. \tag{29}$$

Therefore, EMA describes correctly not only the dispersion and condition for the existence of the TPM, but also its transverse extension into the superlattice quantified by the penetration depth

$$\delta = \frac{1}{\mathrm{Im}\{K\}} = \frac{1}{\mathrm{Im}\{q_{\mathrm{ema}}\}}. \tag{30}$$

The overlap of complex dispersion curves $\beta_{\mathrm{dm}}(\omega)$, $\beta_{\mathrm{TPM}}(\omega)$ and $\beta_{\mathrm{ema}}(\omega)$, corresponding to the single-interface SPP, TPM and the EMA surface wave, is somewhat unexpected considering that it implies an idential modal decay dynamics which is known to be determined by how is the modal energy distributed in space[22]. The fact that these three modes have a very different field variation in the direction perpendicular to the interface while sharing the same dispersion curve is, evidently, a consequence of the simple rule by which the boundary conditions in a two-phase stratified system can be fulfilled, as discussed in Section "Two-phase stratified systems", which allows the ratio of the total field energy residing in the dielectric and metal medium to remain invariant upon the insertion of an arbitrary number interfaces (as long as their total number is odd).

The manner in which the presence of a surface mode modifies the optical properties of an interface is determined by how the reflection coefficient $r(\beta)$, considered as a function over the complex β plane, behaves in the vicinity of the associated pole β_{pole}. For example, ref.[18] shows that the power emitted by a dipole located in the vicinity of a metal-dielectric interface is proportional to the residue a_{pole} of $r(\beta)$ at β_{pole}, evaluated as

$$a_{\mathrm{pole}} = \frac{1}{2\pi \mathrm{i}} \oint_{\gamma} \frac{r(\beta) d\beta}{\beta - \beta_{\mathrm{pole}}}, \tag{31}$$

where γ denotes a positively oriented contour around β_{pole} in the complex β-plane, sufficiently small so that $r(\beta)$ is analytic within it (i.e. avoiding the branch cuts associated with q_i).

The analytic expression for the single-interface SPP residue has been reported in ref.[18]

$$a_{\mathrm{spp}} = \frac{2\varepsilon_1 \varepsilon_2}{\varepsilon_1^2 - \varepsilon_2^2} \beta_{\mathrm{sp}}. \tag{32}$$

Since the homointerface TPM and the EMA surface wave dispersion curves overlap with the SPP, it is straightforward to show that their residues are given by

$$a_{\mathrm{TPM}} = \frac{\sin(q_2 t_2 - q_1 t_1)}{\exp(\mathrm{i} q_1 t_1) \sin(q_2 t_2)} a_{\mathrm{spp}}, \tag{33}$$

where q_1 and q_2 should be evaluated at β_{TPM}, and

$$a_{\mathrm{ema}} = \left(1 + \frac{f}{1-f} \frac{\varepsilon_1}{\varepsilon_2}\right) a_{\mathrm{spp}}, \tag{34}$$

respectively. The last two equations hold only if the mode exists while in case it does not, the corresponding residue is zero.

Comparing the magnitudes of a_{spp}, a_{TPM} and a_{ema} in a $t_{\mathrm{d}} > t_{\mathrm{m}}$ type dielectric-capped superlattice, both $|a_{\mathrm{TPM}}|$ and $|a_{\mathrm{ema}}|$ are seen to decrease monotonously as ω is increased towards ω_{T}, Fig. 5(a) (blue line). This happens because the argument of the sine function in a_{TPM} in Eq. (33) is, according to Eq. (23), proportional to $\varepsilon_{\parallel}$ and thus decreases close to zero (or becomes exactly zero in the lossless limit) at ω_{T}. Since $|a_{\mathrm{ema}}|$ is the limit of $|a_{\mathrm{TPM}}|$ for vanishing layer thicknesses (this holds by definition of EMA and is also evident by taking the $t_i \to 0$ limit of Eq. (33)) it is depicted by dotted lines and indicates the possible trend of the $|a_{\mathrm{TPM}}|$ spectra in case the layer thicknesses are scaled down. Above ω_T, the TPM mode of the dielectric-capped homointerface disappears, meaning

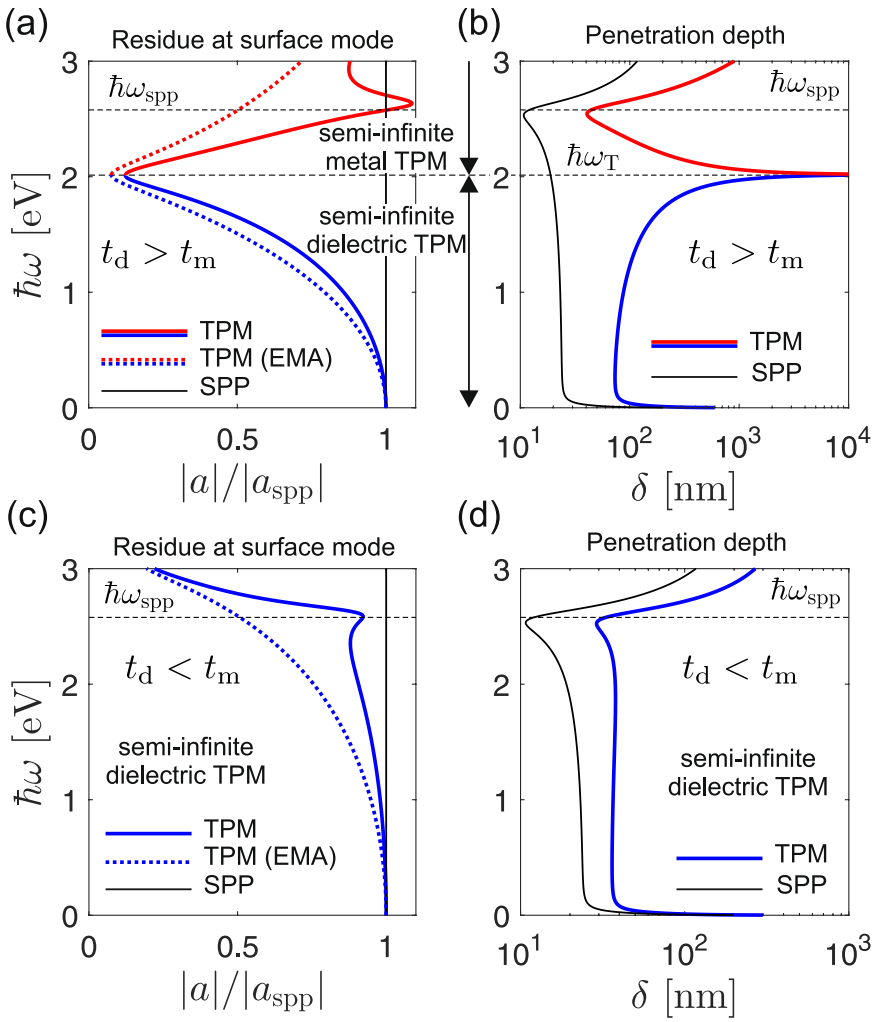

Figure 5. Left panels: residue at the TPM and SPP mode, drawn for the (**a**) $t_d > t_m$ and (**c**) $t_d < t_m$ examples, respectively. Righ panels: penetration depths into the superlattice for (**a**) $t_d > t_m$ and (**c**) $t_d < t_m$ examples, compared with the corresponding SPP penetration depth.

that $|a_{TPM}|$ drops to zero. In order to simplify Fig. 5, the curves corresponding to $|a_{TPM}| = 0$ are omitted, so in Fig. 5(a) the blue and red curves are discontinued at $\omega = \omega_T$. In the lossless limit (not shown), $|a_{TPM}|$ becomes exactly zero at ω_T.

The opposite trend of $|a_{TPM}|$ is observed for the $t_d > t_m$ type metal-capped superlattice, where $|a_{TPM}|$ starts from small values (zero in the lossless limit) at ω_T and approaches $|a_{spp}|$ as ω goes to ω_{spp}. The disappearance of the TPM resonance around ω_T is accompanied with a delocalization of the mode energy across the superlattice, as seen in Fig. 5(b). In the lossless limit, the penetration depth δ of the TPM mode diverges at ω_T, while in the real lossy case shown in Fig. 5(b), δ reaches values up to around 10 microns. The penetration depth of the single-interface SPP shown for reference (black line), varies only a bit between 20 and 30 nm over the infrared and visible frequencies, up to ω_{spp} where it has a dip.

For the $t_d < t_m$ class of superlattices, a simpler behavior is found, as depicted in Fig. 5(c) and (d). Here $|a_{TPM}|$ is only slightly below $|a_{spp}|$, while the TPM penetrates only slightly more into the superlattice, showing no pronounced spectral variations.

Figures 5(a) and (c) show that the EMA description of homointerface TPMs is not entirely accurate, after all. The fact that a_{ema} differs from a_{TPM} means that EMA does not account properly for the TPM contribution to the reflection coefficient, meaning the it will give an erroneous TPM dispersion if any additional interface is added, as it is the case with a heterointerface.

Heterointerface. A heterointerface is obtained when the capping medium permittivity ε_a differs from the permittivities ε_1, ε_2 of the two superlattice constituents, as shown in Fig. 6. The notation is chosen so that ε_1 denotes the permittivity of the top layer of the superlattice, which is shown below to play a major role in determining the types of TPMs supported by the interface. Denoting by a and b the plane wave amplitudes of the incoming and scattered wave, the heterointerface reflection coefficient r_{het} is defined as their ratio for excitation from the capping medium. Introducing the auxiliary reflection coefficient

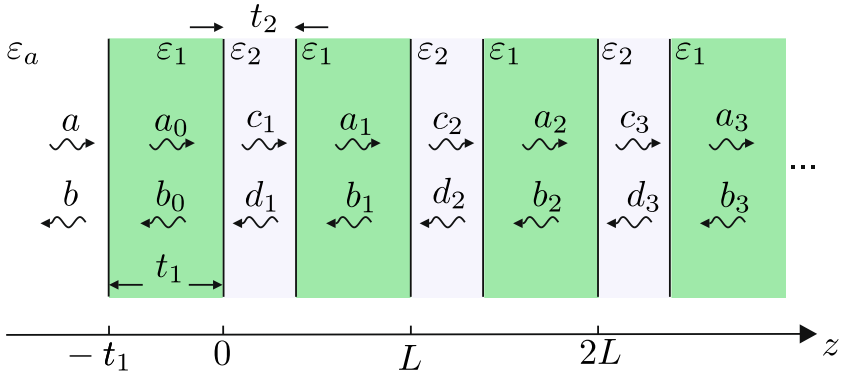

Figure 6. Schematics of the heterointerface geometry. It is obtained from the homointerface geometry in Fig. 4 by replacing the semi-infinite ε_1 medium with a semi-infinite medium ε_a extending from left infinity up to $z = -t_1$, so that the structure remains invariant for $z > -t_1$. In the text we show that the TPM properties are determined by a combined interaction of the newly added $\varepsilon_a - \varepsilon_1$ interface at $z = -t_1$ and the homointerface at $z = 0$ buried under the top ε_1 layer of the superlattice.

$$r_a = \frac{\alpha_a - \alpha_1}{\alpha_a + \alpha_1}, \tag{35}$$

which corresponds to reflection on a single interface between ε_a and ε_1, the total reflection coefficient is obtained as

$$r_{\text{het}} = \frac{r_a + r\exp(2iq_1t_1)}{1 + r_a r\exp(2iq_1t_1)}. \tag{36}$$

The condition for the existence of a TPM mode in the non-trivial case ($r_a \neq 0$ and $r \neq 0$) is that the denominator vanishes

$$1 + r_a r\exp(2iq_1t_1) = 0, \tag{37}$$

where we recognize the typical condition for a cavity resonance, with r_a and r being the mirror reflection coefficients. In ultrathin films considered here, the real part of phase $2q_1t_1$ is much below π, meaning that the heterointerface TPMs are not expected to have a Fabri-Perot character but to be formed by the modification of poles of either r_a or r, as the rapid variation of the reflection phase in their vicinity allows the condition in Eq. (37) to be satisfied.

For a given frequency ω, the complex in-plane wavenumber of a TPM fulfilling Eq. (37) will be denoted by $\beta_n(\omega)$, with $n = 1, 2, \ldots$ enumerating the existing TPMs. In contrast to the homointerface case in which only one TPM is allowed while the dependence of β_{TPM} on ω is given by an analytic expression, here multiple solutions may exist while $\beta_n(\omega)$ cannot, in principle, be expressed analytically. Therefore, we look for TPM modes by evaluating $r_{\text{het}}(\omega, \beta)$ in the $\beta - \omega$ plane[19] and use the fact that the local density of optical states $\rho(\omega, \beta)$ at the interface is proportional[25] to the imaginary part of r_{het}, so that sharp maxima of $|\text{Im}\{r_{\text{het}}\}|$ signal the presence of a TPM.

Typical r_{het} maps for $t_d > t_m$ heterointerface types are depicted in Fig. 7(a–d), with lossless single-interface $\varepsilon_d - \varepsilon_m^{(0)}$ and $\varepsilon_a - \varepsilon_m^{(0)}$ SPP dispersion curves denoted by $\beta_{md}(\omega)$ and $\beta_{am}(\omega)$ drawn for reference. In order to sharpen the map features, we compare the maps corresponding the actual silver permittivity ε_m (right panels of Fig. 7) with ones obtained by assuming reduced losses, i.e. $\varepsilon_m^{(p)}$ with $p < 1$. Here we use $p = 0.1$, as it is found to be sufficient for reliably resolving the TPM dispersion in the $\beta - \omega$ plane. As expected, the $|\text{Im}\{r_{\text{het}}\}|$ has higher values within the bands, and decreases rapidly with crossing the band edges indicated by thin (black) solid lines. The TPM modes show up as dark bands in the $\beta - \omega$ plane outside of the bulk bands.

A formal justification for relating the properties of the two maps is based on perturbation theory[22] which shows that, up to the first order, the real part of the modal wavenumber $\text{Re}\{\beta_n\}$ is independent on the perturbation parameter $g = \text{Im}\{\varepsilon_m\}/\varepsilon_m$, while $\text{Im}\{\beta_n\}$ has a linear proportionality. Therefore, the sharp maps in the left panels of Fig. 7 are used for estimating the complex β_n. The estimated value is then used as a starting guess for a Nelder-Mead minimization method[26] implemented numerically, which finds the solutions for β_n, with high accuracy, as the minima of the absolute value of the left-hand side in Eq. (37).

In the case of a metallic top layer of the $t_d > t_m$ heterointerface, two TPM modes, TPM-1 and TPM-2, are identified, as indicated by thick enumerated (red) lines in Fig. 7(b). The curves representing $\text{Re}\{\beta_1(\omega)\}$ and $\text{Re}\{\beta_2(\omega)\}$ are seen to correspond well to the sharp peaks in the vicinity of $\beta_{am}(\omega)$ and $\beta_{md}(\omega)$ curves in Fig. 7(a). At first, it might apear unusual that we do not consider the dark band in Fig. 7(a) appearing slightly above $\omega_{spp,a}$ and having a negative slope. We have found that, although formally a TPM mode, it is so far from the real β-axis that the associated propagation length is in the nanometer range, which makes it effectively indistinguishable from the air-silver surface plasmon resonance. The fact that this band appears as sharp in Fig. 7(a) as TPM-1 and TPM-2, while numerical calculations show it is dissipated much more, indicates that the perturbation picture does not

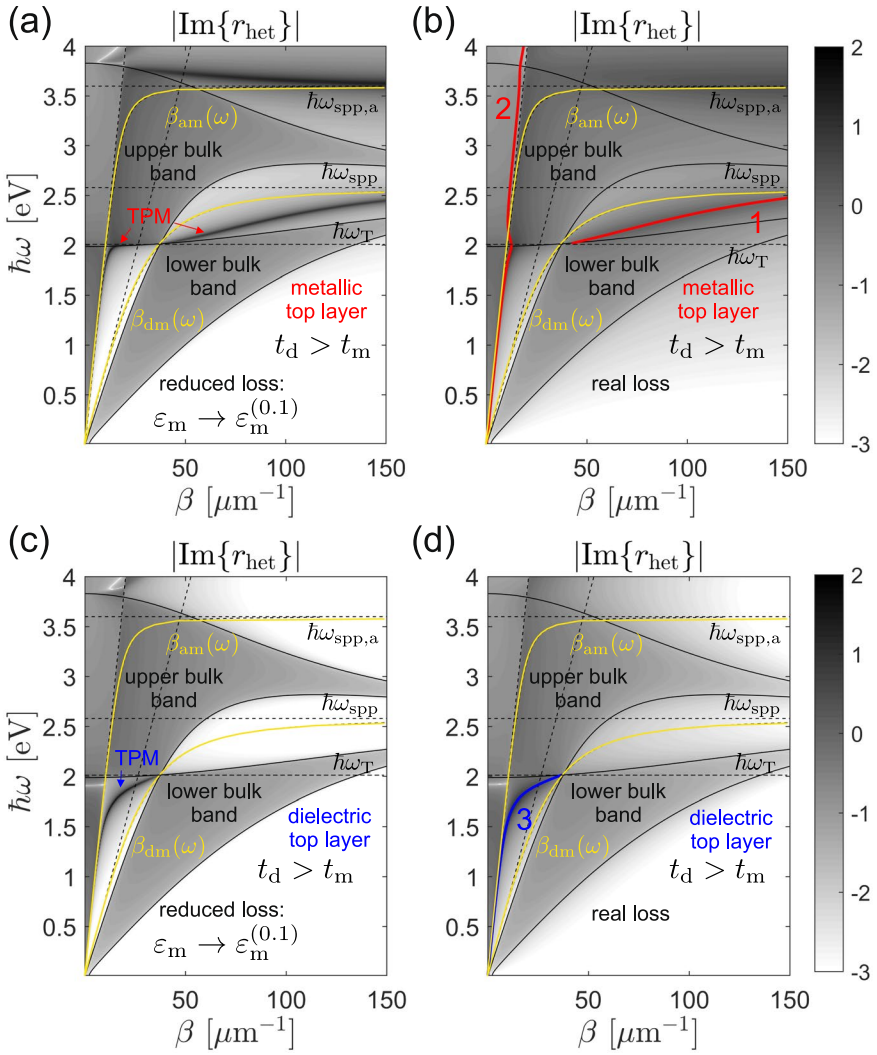

Figure 7. Maps of $|\mathrm{Im}\{r_{\mathrm{het}}\}|$ drawn in logarithmic scale with the colormap chosen so that all values outside the $(-3, 2)$ interval are saturated. Top panels are drawn for superlattices terminated by a metallic layer ($\varepsilon_1 = \varepsilon_{\mathrm{m}}$), while the bottom ones correspond to a dielectric top layer ($\varepsilon_1 = \varepsilon_{\mathrm{d}}$). Left panels: maps obtained by multiplying the imaginary part of the silver permittivity by $p = 0.1$ in order to sharpen the features and render TPMs visible. Right panels: maps obtained by taking the loss fully into account. All maps correspond to the $t_{\mathrm{d}} > t_{\mathrm{m}}$ example. The two slanted dashed lines represent the ε_a and ε_{d} light lines.

work well above the top bulk band. Indeed, in the vicinity of $\omega_{\mathrm{spp,a}}$ the real and the imaginary part of ε_{m} have comparable magnitudes, meaning that $|g|$ is not small compared to unity as required by perturbation theory[22].

The fact that TPM-1 and TPM-2 in Fig. 7(b) arise by a modification of the metal-capped homointerface TPM and the single-interface $\varepsilon_a - \varepsilon_{\mathrm{m}}$ SPP, respectively, can be shown by considering Eq. (37). Assuming first that $|r_a \exp(2iq_1t_1)|$ is small around the $\beta_{\mathrm{TPM}}(\omega)$ pole of r, so that the $\beta_1(\omega)$ pole of r_{het} is close to $\beta_{\mathrm{TPM}}(\omega)$, r can be written as

$$r(\omega, \beta) \approx \frac{a_{\mathrm{TPM}}}{\beta - \beta_{\mathrm{TPM}}(\omega)}, \tag{38}$$

which combined with Eq. (37) yields

$$\beta_1(\omega) \approx \beta_{\mathrm{TPM}}(\omega) - a_{\mathrm{TPM}} r_a \exp(2iq_1t_1). \tag{39}$$

This shows that if the heterointerface is obtained by gradually changing the capping permittivity from ε_1 to ε_a, the dispersion curve $\beta_1(\omega)$ gradually evolves from $\beta_{\mathrm{TPM}}(\omega)$, with a deviation increasing as r_a increases and with a factor proportional to the homointerface TPM residue a_{TPM}. Another important implication of Eq. (39) is that using EMA does not yield a correct dispersion of heterointerface TPMs because a_{ema} differs from a_{TPM}.

Repeating a similar analysis but now assuming $\beta_2(\omega)$ is in the vicinity of $\beta_{\mathrm{am}}(\omega)$, we find

$$\beta_2(\omega) \approx \beta_{\mathrm{am}}(\omega) - a_{\mathrm{spp},a} r \exp(2iq_1t_1), \tag{40}$$

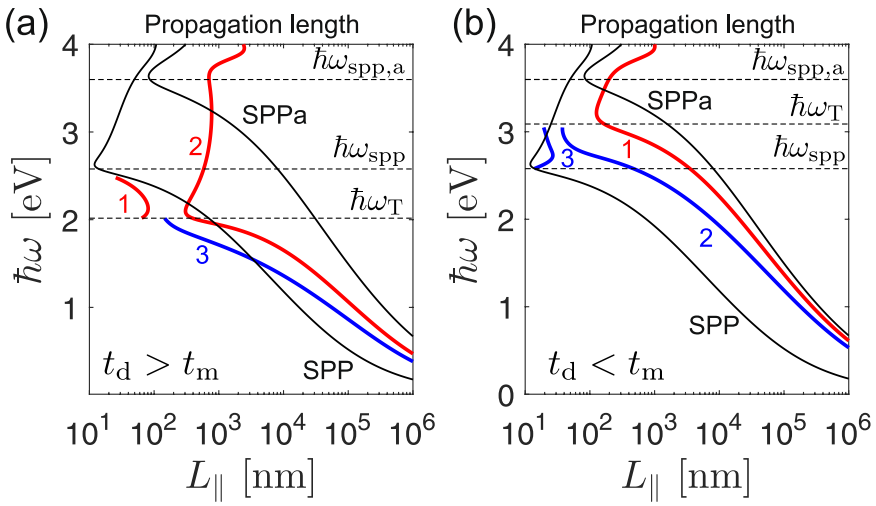

Figure 8. In-plane propagation length $L_{\parallel}$ for TPMs whose dispersion of $\mathrm{Re}\{\beta_n(\omega)\}$ is drawn in (**a**) Figs 7 and (**b**) and 9. The solid lines denoted as SPP and SPPa are the $L_{\parallel}$ values corresponding to the $\varepsilon_{\mathrm{d}}-\varepsilon_{\mathrm{m}}$ and $\varepsilon_{\mathrm{a}}-\varepsilon_{\mathrm{m}}$ interface SPPs.

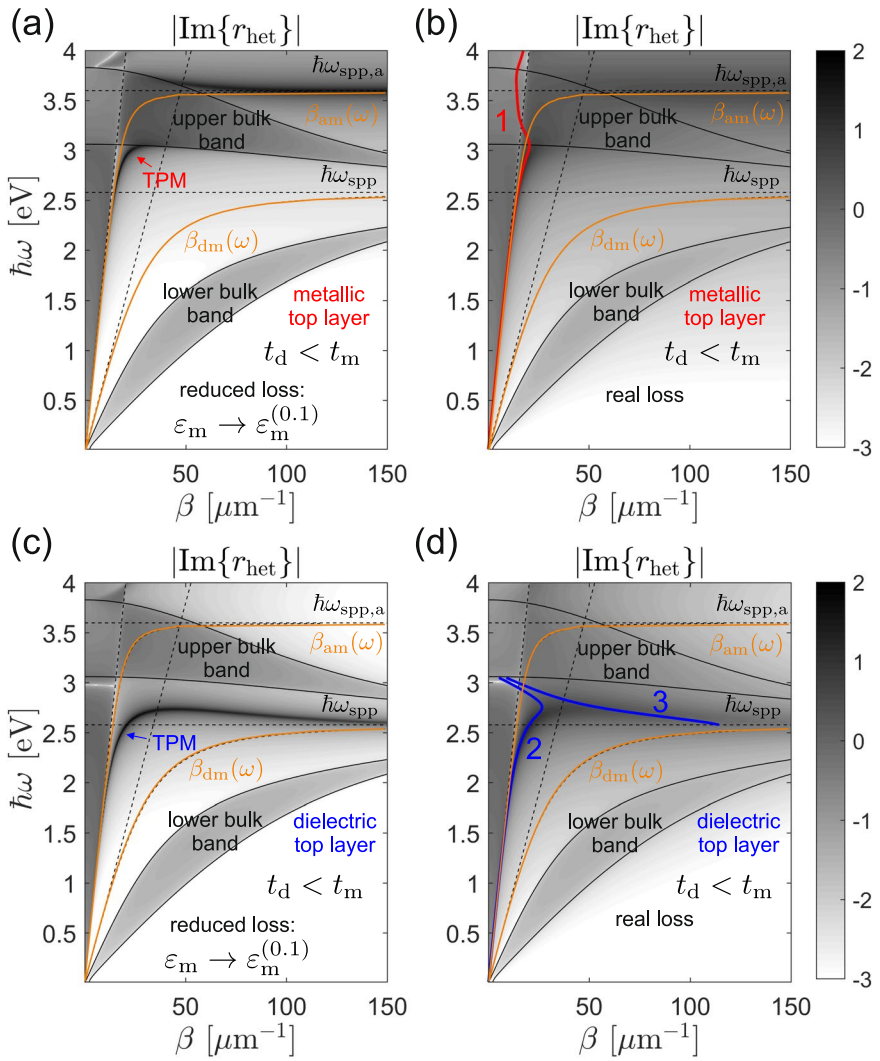

Figure 9. Maps of $|\mathrm{Im}\{r_{\mathrm{het}}\}|$ fully analogous to those drawn in Fig. 7, except that here the $t_{\mathrm{d}} < t_{\mathrm{m}}$ example is considered.

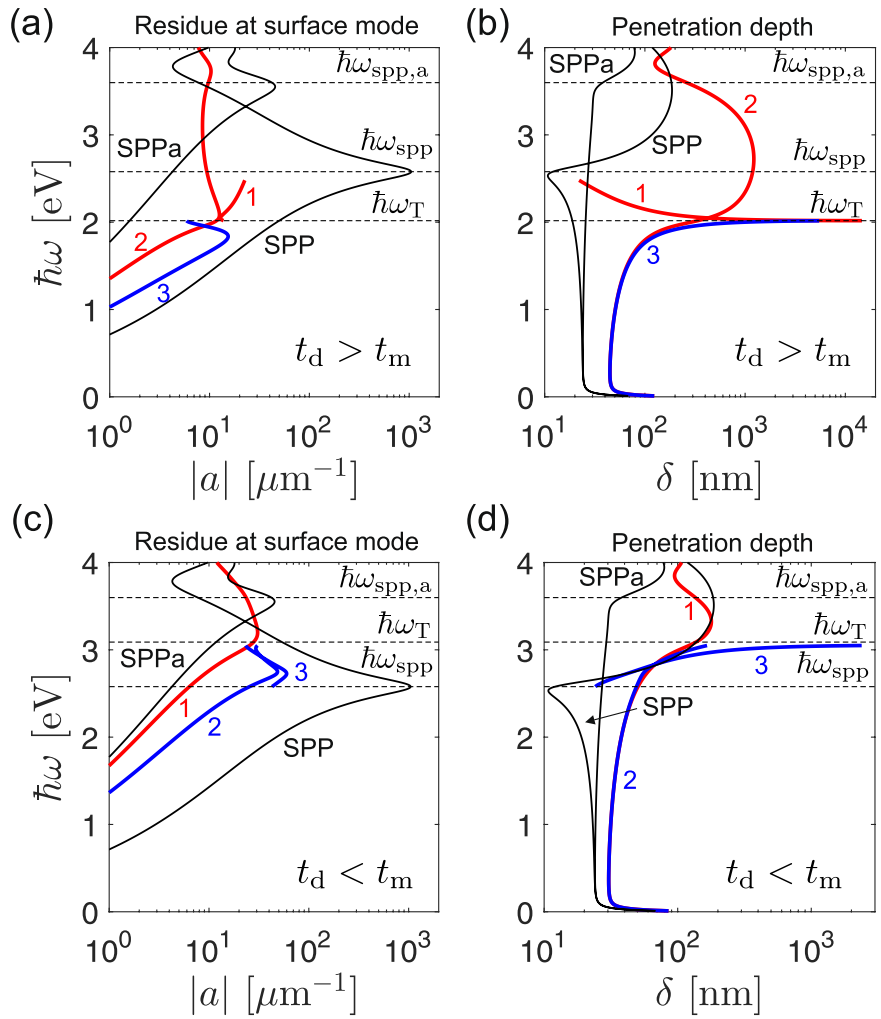

Figure 10. Left panels: residue at the TPM and SPP modes, drawn for the (**a**) $t_d > t_m$ and (**c**) $t_d < t_m$ examples, respectively. Righ panels: penetration depths into the superlattice for (**b**) $t_d > t_m$ and (**d**) $t_d < t_m$ examples, compared with the corresponding SPP penetration depth. SPP and SPPa stand for the $\varepsilon_d - \varepsilon_m$ and $\varepsilon_a - \varepsilon_m$ interface SPPs, respectively.

which shows that $\beta_2(\omega)$ will be very close to $\beta_{am}(\omega)$ if $|r \exp(2iq_1t_1)|$ is small which e.g. is a good approximation for $t_1 = t_m = 20$ nm, or higher. Equations (39) and (40) thus allow us to classify the heterointerface TPMs into homointerface-like (TPM-1) and SPP-like (TPM-2).

The bottom two panels of Fig. 7 show the case in which the $t_d > t_m$ superlattice is terminated by the dielectric layer. Here only one solution, TPM-3, exists which evidently originates from the dielectric-capped homointerface TPM meaning it falls under the homointerface-like TPM type.

The thick TPM dispersion curves in Fig. 7 show the real part of the modal in-plane wavenumber β_n. The corresponding imaginary parts determine the lateral propagation length of the mode

$$L_{\parallel,n} = \frac{1}{\mathrm{Im}\{\beta_n\}}. \tag{41}$$

The values obtained for the realistic (lossy) case are shown in Fig. 8(a), together with reference values corresponding to SPPs on $\varepsilon_d - \varepsilon_m$ (denoted as SPP) and $\varepsilon_a - \varepsilon_m$ (denoted as SPPa) single interfaces. At lower frequencies, both TPM-2 and TPM-3 are seen to have $L_{\parallel}$ values between the two single-interface SPP limits. As ω_T is approached, the propagation length of TPM-3 drops which is a result of the reduced group velocity, cf. the reduced slope of TPM-3 in the vicinity of ω_T in Fig. 7(d). The $L_{\parallel}$ value of TPM-2 also drops above ω_T, but here the reason is that it hybridizes with bulk modes in the superlattice and free space modes in the ε_a light cone and leaks away from the surface, cf. Fig. 7(b) where the thick (red) line denoted by 2 is seen to enter the ε_a lightcone once it enters the upper bulk band. Finally, TPM-1 is seen to have extremely low propagation lengths (below 100 nm) over the entire spectrum in which it is supported, which is the concequence of the vicinity of the SPP resonance at ω_{spp}.

Analogous r_{het} maps obtained for the $t_d < t_m$ example are plotted in Fig. 9(a–d). As here $\omega_T > \omega_{spp}$, homointerface-like TPMs appear only in the case of a dielectric top layer, as indicated by the TPM-2 and TPM-3

lines in Fig. 9(d). The shape of the TPM band indicated in Fig. 9(c) shows that the effect of replacing titanium dioxide by air as the capping medium blueshifts the homointerface TPM and deforms it so that its slope becomes zero around $\beta \approx 35\,\mu\text{m}^{-1}$ and negative for larger β. This implies that at frequencies slightly above ω_{spp} there are two TPM modes, which is confirmed by the numerically found TPM-2 and TPM-3 dispersion curves in Fig. 9(d). Here it should be noted that the TPM-3 curve represents $-\text{Re}\{\beta_3\}(\omega)$, i.e. the actual dispersion curve lying in the $\beta < 0$ half-space is folded to the positive sided for a compact representation, see also refs[22,23], for further discussion of this topic.

The TPM mode of the $t_d < t_m$ superlattice with metallic top layer is a modified $\varepsilon_a - \varepsilon_m$ single-interface SPP, as evident from its dispersion in Fig. 9(a) and (b), where it is seen to closely follow the $\beta_{am}(\omega)$ curve, up until hybridizes with modes from the upper bulk band after which the pole shifts into the ε_a light cone and starts leaking out into both the superlattice and capping layer propagating modes. The propagation lengths of the TPM modes of the $t_d < t_m$ example are shown in Fig. 8(b).

The resonance strength and confinement degree of heterointerface TPM modes for the considered two superlattice types is summarized in Fig. 10(a–d). Perhaps the most relevant case is that of the $t_d > t_m$ supperlattice with a dielectric top layer supporting TPM-3 depicted in Fig. 10(a). Similarly as its homointerface counterpart, by the perturbation of which TPM-3 is formed, the resonance strength of this mode is seen to rapidly decrease as ω_T is approached while it becomes delocalized across the superlattice, as seen in Fig. 10(c).

Summary and conclusion. This paper presents a systematic analysis of surface waves on two-phase semi-infinite metallodielectric superlattices. As their character is determined by the properties of the periodic arrangement of unit cells, in analogy with surface electronic states in crystals, these waves are termed Tamm plasmon modes.

It is shown that if the capping medium has the same permittivity as one of the superlattice constituents, a case referred to as the homointerface, TPM modes can exist only along the single-interface SPP dispersion curve and that there exists a critical frequency ω_T which represents the upper limit for the TPM existence in the dielectric- and the lower frequency limit in the metal-capped superlattice and is determined by the superlattice composition and relative layer thicknesses. This fact is particularly relevant if ω_T is below the SPP resonance frequency, which happens if the dielectric layers are thicker than the metal layers. Both the dielectric- and metal-capped TPMs become delocalized across the lattice when ω_T is approached, while the strength of the corresponding resonance, quantified by residues of the reflection coefficient at the associated poles, dies out.

The heterointerface, where the capping medium permittivity differs from that of the superlattice constituents and most relevant in practice as it includes the case of the superlattice exposed to air, is found to be exhibit a more complex behavior. We show that the heterointerface TPMs can be analyzed as resulting from either the capping-top layer interface, or an homointerface TPM located at the interface between the top layer and the rest of the superlattice. The homointerface-like TPMs, originating from the latter group, are found to also exhibit the critical behaviour around ω_T.

In view of the significance of the effective medium approximation for the ongoing research on hyperbolic metamaterials, we have also compared its predictions against the exact theory. Somewhat surprisingly, we find that EMA accurately describes several important aspects of homointerface TPMs with arbitrary layer thicknesses, including the critical behaviour, but that it fails entirely in the heterointerface case.

These results are important for engineering the optical properties of semi-infinite metallodielectric superlattices which have recently been receiving strong attention in connection with enhanced spontaneous emission into the bulk superlattice modes. The analysis reported here should help quantify the individual contributions of the bulk and TPM modes in the total optical density of states at the interface and thus tailor the amount of emitted light that propagates through the superlattice or stays tied at the interface, respectively.

References

1. Cai, W. & Shalaev, V. *Optical Metamaterials* (Springer, New York, 2010).
2. Maier, S. A. *Plasmonics: Fundamentals and Applications* (Springer, 2007).
3. Poddubny, A., Iorsh, I., Belov, P. & Kivshar, Y. Hyperbolic metamaterials. *Nat. Photon.* **7**, 948–957 (2013).
4. Chen, W., Thoreson, M. D., Ishii, S., Kildishev, A. V. & Shalaev, V. M. Ultra-thin ultra-smooth and low-loss silver films on a germanium wetting layer. *Opt. Express* **18**, 5124–5134 (2010).
5. Jacob, Z. *et al*. Engineering photonic density of states using metamaterials. *Appl. Phys. B* **100**, 215–218 (2010).
6. Jacob, Z., Smolyaninov, I. I. & Narimanov, E. E. Broadband purcell effect: Radiative decay engineering with metamaterials. *Appl. Phys. Lett.* **100**, 181105 (2012).
7. Ferrari, L., Wu, C., Lepage, D., Zhang, X. & Liu, Z. Hyperbolic metamaterials and their applications. *Prog. Quant. Electron.* **40**, 1–40 (2015).
8. Kaliteevski, M. *et al*. Tamm plasmon-polaritons: Possible electromagnetic states at the interface of a metal and a dielectric bragg mirror. *Phys. Rev. B* **76**, 165415 (2007).
9. Sasin, M. E. *et al*. Tamm plasmon polaritons: Slow and spatially compact light. *Appl. Phys. Lett.* **92**, 251112 (2008).
10. Gazzano, O. *et al*. Evidence for confined tamm plasmon modes under metallic microdisks and application to the control of spontaneous optical emission. *Phys. Rev. Lett.* **107**, 247402 (2011).
11. Symonds, C. *et al*. Confined tamm plasmon lasers. *Nano Lett.* **13**, 3179–3184 (2013).
12. Zhang, C., Wu, K., Giannini, V. & Li, X. Planar hot-electron photodetection with tamm plasmons. *ACS Nano* **11**, 1719–1727 (2017).
13. Zhang, W. L., Wang, F., Rao, Y. J. & Jiang, Y. Novel sensing concept based on optical tamm plasmon. *Opt. Express* **22**, 14524–14529 (2014).
14. Das, R., Srivastava, T. & Jha, R. Tamm-plasmon and surface-plasmon hybrid-mode based refractometry in photonic bandgap structures. *Opt. Lett.* **39**, 896–899 (2014).
15. Krishnamoorthy, H., Jacob, Z., Narimanov, E., Kretzschmar, I. & Menon, V. Topological transitions in metamaterials. *Science* **336**, 205–209 (2012).
16. Kidwai, O., Zhukovsky, S. V. & Sipe, J. E. Effective-medium approach to planar multilayer hyperbolic metamaterials: Strengths and limitations. *Phys. Rev. A* **85**, 053842 (2012).

17. Newman, W. D., Cortes, C. L. & Jacob, Z. Enhanced and directional single-photon emission in hyperbolic metamaterials. *J. Opt. Soc. Am. B* **30**, 766–775 (2013).
18. Ford, G. & Weber, W. Electromagnetic interactions of molecules with metal surfaces. *Phys. Rep.* **113**, 195–287 (1984).
19. Isić, G. & Gajić, R. Lifetime and propagation length of light in nanoscopic metallic slots. *J. Opt. Soc. Am. B* **31**, 393–399 (2014).
20. Yeh, P., Yariv, A. & Hong, C.-S. Electromagnetic propagation in periodic stratified media. i. general theory. *J. Opt. Soc. Am.* **67**, 423–438 (1977).
21. Rakic, A. D., Djurisic, A. B., Elazar, J. M. & Majewski, M. L. Optical properties of metallic films for vertical-cavity optoelectronic devices. *Appl. Opt.* **37**, 5271–5283 (1998).
22. Isić, G., Gajić, R. & Vuković, S. Plasmonic lifetimes and propagation lengths in metallodielectric superlattices. *Phys. Rev. B* **89**, 165427 (2014).
23. Rosenblatt, G. & Orenstein, M. Competing coupled gaps and slabs for plasmonic metamaterial analysis. *Opt. Express* **19**, 20372–20385 (2011).
24. Born, M. & Wolf, E. *Principles of optics* (Cambridge University Press, 2005).
25. Novotny, L. & Hecht, B. *Principles of Nano-Optics* (Cambridge University Press, 2012).
26. Nelder, J. A. & Mead, R. A simplex method for function minimization. *Comput. J.* **7**, 308–313 (1965).

Acknowledgements

This work was supported by the Serbian Ministry of Education, Science and Technological Development under Projects No. ON171005, III45016 and TR32008, as well as by Qatar National Research Fund under project NPRP 8-028-1-001. This work was performed in the context of the European COST Action MP1302 Nanospectroscopy.

Author Contributions

S.V. and G.I. conceived the analysis, G.I. conducted the numerical calculations, All authors discussed the results and reviewed the manuscript.

Additional Information

Competing Interests: The authors declare that they have no competing interests.

Publisher's note: Springer Nature remains neutral with regard to jurisdictional claims in published maps and institutional affiliations.